Reaction of O_2 with a diiron protein generates a mixed-valent Fe^{2+}/Fe^{3+} center and peroxide

Justin M. Bradley[a], Dimitri A. Svistunenko[b], Jacob Pullin[b], Natalie Hill[a], Rhona K. Stuart[c,1], Brian Palenik[c], Michael T. Wilson[b], Andrew M. Hemmings[a,d], Geoffrey R. Moore[a], and Nick E. Le Brun[a,2]

[a]Centre for Molecular and Structural Biochemistry, School of Chemistry, University of East Anglia, Norwich NR4 7TJ, United Kingdom; [b]School of Biological Sciences, University of Essex, Colchester CO4 3SQ, United Kingdom; [c]Scripps Institution of Oceanography, University of California, San Diego, La Jolla, CA 92093; and [d]School of Biological Sciences, University of East Anglia, Norwich NR4 7TJ, United Kingdom

Edited by Amy C. Rosenzweig, Northwestern University, Evanston, IL, and approved December 12, 2018 (received for review June 8, 2018)

The gene encoding the cyanobacterial ferritin *Syn*Ftn is up-regulated in response to copper stress. Here, we show that, while *Syn*Ftn does not interact directly with copper, it is highly unusual in several ways. First, its catalytic diiron ferroxidase center is unlike those of all other characterized prokaryotic ferritins and instead resembles an animal H-chain ferritin center. Second, as demonstrated by kinetic, spectroscopic, and high-resolution X-ray crystallographic data, reaction of O_2 with the di-Fe^{2+} center results in a direct, one-electron oxidation to a mixed-valent Fe^{2+}/Fe^{3+} form. Iron–O_2 chemistry of this type is currently unknown among the growing family of proteins that bind a diiron site within a four α-helical bundle in general and ferritins in particular. The mixed-valent form, which slowly oxidized to the more usual di-Fe^{3+} form, is an intermediate that is continually generated during mineralization. Peroxide, rather than superoxide, is shown to be the product of O_2 reduction, implying that ferroxidase centers function in pairs via long-range electron transfer through the protein resulting in reduction of O_2 bound at only one of the centers. We show that electron transfer is mediated by the transient formation of a radical on Tyr40, which lies ∼4 Å from the diiron center. As well as demonstrating an expansion of the iron–O_2 chemistry known to occur in nature, these data are also highly relevant to the question of whether all ferritins mineralize iron via a common mechanism, providing unequivocal proof that they do not.

diiron protein | ferritin | iron | tyrosyl radical | electron transfer

Ferritins constitute a ubiquitous family of proteins found in all domains of life. They are rhombic dodecahedral 24-mer protein assemblies that delimit a central cavity in which a ferric-oxy mineral can be reversibly deposited (1–3). They provide a means for storage, buffering, and detoxification of iron, contributing to cellular iron management and the alleviation of oxidative stress. Animal ferritins are, in general, heteropolymers composed of two types of subunits, H- and L-chains. H-chain ferritins contain a diiron site, termed the ferroxidase center, at which the rapid oxidation of Fe^{2+} to Fe^{3+} is coupled to O_2 reduction. L-chain ferritins lack this catalytic center but are thought to promote nucleation of the mineral core via a carboxylate-rich patch located on the inner surface of the protein nanocage (4, 5). The subunit composition of animal ferritins is dependent on the tissue from which the protein was isolated (2).

The genomes of plants and prokaryotes often encode more than one predicted ferritin, of which all differ from their eukaryotic counterparts in that they are composed solely of H-chain–like subunits containing iron-binding catalytic centers. Other than in the distinct subset of heme-binding bacterioferritins, the amino acid side chains ligating these two iron atoms are highly conserved. The major structural difference between the catalytic centers of prokaryotic, animal, and plant (phyto) ferritins is the presence of a third iron binding site, termed site C, ∼6 Å from the diiron site of the prokaryotic ferritin (Ftn) (6). Both phytoferritin and animal H-chain subunits lack this third iron binding site, and phytoferritin contains the carboxylate-rich patch associated with the animal L-chains, which is absent from both animal H-chains and Ftn (3). Therefore, the heme-free ferritins can be classified as animal-, prokaryotic-, or plant-like by considering the subunit composition together with the presence or absence of a site C or a carboxylate-rich patch. However, despite differences in structure, composition, and mechanistic detail, all of these proteins share a common first step in their reaction cycle; namely, the formation of an unstable diferric-peroxo (DFP) intermediate that decays to yield a ferric-oxo mineral precursor (7).

Cyanobacteria are photosynthetic organisms that play a critical role in the carbon cycle. Marine picocyanobacteria, including *Synechococcus* and *Prochlorococcus*, alone are estimated to account for a minimum of 20% of all global carbon fixation (8). Coastal-dwelling *Synechococcus* strains exhibit greater tolerance to metal stress than their ocean-dwelling counterparts. This tolerance is due to the presence of a greater number of genes involved in metal ion homeostasis, most likely as a consequence of the evolutionary pressures exerted by seasonal variations in the metal ion content of their habitat (9). An unusual example is the response of the coastal *Synechococcus* strain CC9311 to copper stress and associated oxidative stress, which involves the up-regulation of the predicted ferritin sync_1539, hereto referred to as *Syn*Ftn (9). Up-regulation of a predicted ferritin was unexpected because they are typically expressed in response to iron

Significance

Enzymes that activate dioxygen at diiron centers located within four α-helical bundles with carboxylate residue-rich coordination are abundant in nature. Mechanistic studies of the Fe^{2+}/Fe^{2+} forms of these proteins have shown that peroxo-Fe^{3+}/Fe^{3+} intermediates are common to most of their reactions. Remarkably, the O_2 reaction of the unusual ferritin *Syn*Ftn does not lead to the peroxo-Fe^{3+}/Fe^{3+} form but instead directly generates mixed-valent Fe^{3+}/Fe^{2+} centers and hydrogen peroxide via a mechanism that involves long-range electron transfer between diiron centers and the transient formation of a Tyr• radical close to the diiron center. This work reveals previously unrecognized catalytic iron–O_2 chemistry and demonstrates that ferritins do not all mineralize iron via a common mechanism.

Author contributions: J.M.B., B.P., and N.E.L.B. designed research; J.M.B., D.A.S., J.P., N.H., R.K.S., M.T.W., and A.M.H. performed research; J.M.B., D.A.S., M.T.W., and A.M.H. analyzed data; and J.M.B., D.A.S., R.K.S., B.P., G.R.M., and N.E.L.B. wrote the paper.

The authors declare no conflict of interest.

This article is a PNAS Direct Submission.

Data deposition: The atomic coordinates and structure factors have been deposited in the Protein Data Bank, www.wwpdb.org (PDB ID codes 5OUW, 6GKC, 6GKA, 5OUZ, and 6GKB).

[1] Present address: Biosciences and Biotechnology Division, Lawrence Livermore National Laboratory, Livermore, CA 94550.

[2] To whom correspondence should be addressed. Email: n.le-brun@uea.ac.uk.

This article contains supporting information online at www.pnas.org/lookup/suppl/doi:10.1073/pnas.1809913116/-/DCSupplemental.

www.pnas.org/cgi/doi/10.1073/pnas.1809913116

(10). Furthermore, *Syn*Ftn was detected in the exoproteome of *Synechococcus* CC9311 (11), raising the possibility that this ferritin is localized, at least in part, outside of the cytoplasm, again suggestive of a role other than regulation of iron concentration within the cell.

Here, we report optical and magnetic spectroscopic, kinetic, and high-resolution structural studies of *Syn*Ftn, revealing that the O_2-driven oxidation of the Fe^{2+}/Fe^{2+} form does not result in a (per)oxo-Fe^{3+}/Fe^{3+} intermediate as it does in all other characterized ferritins, and most other carboxylate-bridged diiron centers. Instead, *Syn*Ftn directly generates a mixed-valent Fe^{3+}/Fe^{2+} form along with hydrogen peroxide. Furthermore, the data demonstrate the formation of a transient radical on Tyr40, which is essential for rapid Fe^{2+} oxidation. These data lead to a mechanistic model in which diiron centers cooperate via long-range electron transfer to reduce a single O_2 molecule bound at one with formation of two mixed-valent diiron centers. The physiological significance of these observations is discussed.

Results

SynFtn Is a Functional Prokaryotic Ferritin with a Eukaryotic-Like Active Site. Purified *Syn*Ftn behaved as a typical 24-mer ferritin when examined by size-exclusion chromatography and native PAGE (*SI Appendix*, Fig. S1*A*). However, alignment of its amino acid sequence with those of other ferritins showed that the residues comprising site C in all prokaryotic ferritins characterized to date are absent (*SI Appendix*, Fig. S1*B*). The 2.05-Å crystal structure of *Syn*Ftn (*SI Appendix*, Fig. S1 *C* and *D* and Table S1) showed that each of the 24 subunits adopts the characteristic four α-helical bundle motif of the ferritin family and their assembly into a 24-meric protein cage with the expected 4–3–2 symmetry. The protein as crystalized was free of metal ions, but the disposition of the conserved ferroxidase center ligands suggested that it would be capable of binding two metal ions without major structural rearrangement (Fig. 1*A*).

The interactions of the protein with iron were assessed in solution. Absorbance monitored iron mineralization assays demonstrated that *Syn*Ftn was capable of laying down a mineral core containing up to 2,000 Fe^{3+} per protein cage (Fig. 2*A*) at a rate greater than that of *Escherichia coli* FtnA (12) or *Pyrococcus furiosus* Ftn (13), the most intensively studied of the Ftns, and similar to that of homopolymers of animal H-chains (4). The rate increased with pH consistent with the release of protons during mineralization, as reported for other ferritins (1). Interactions of *Syn*Ftn with copper were also investigated because expression of the gene encoding it was up-regulated in response to this metal. A total of 400 copper ions (as 200 μM Cu^{2+} or Cu^{+}) was added per *Syn*Ftn and incubated for 60 min aerobically (Cu^{2+}, Cu^{+}) or anaerobically (Cu^{+}) before removal of unbound copper via a desalting column. Residual copper concentrations determined were 2 ± 1 μM (anaerobic Cu^{+}), 3 ± 1 μM (aerobic Cu^{+}), and 5 ± 2 μM (aerobic Cu^{2+}), while that determined for a protein free Cu^{2+} control was 3.0 ± 1.0 μM. Incorporation of copper into the mineral core during deposition was probed by the same assay method, but using 4.1 μM *Syn*Ftn incubated aerobically with 1.6 mM Fe^{2+} and 200 μM of either Cu^{+} or Cu^{2+}. Copper concentrations determined were 5 ± 2 μM (Cu^{2+}) and 6 ± 3 μM (Cu^{+}) compared with 3 ± 1 μM in protein free controls, and we therefore conclude that copper is not incorporated into the ferric mineral core of *Syn*Ftn. Thus, in contrast to iron, there is no direct interaction between copper, either as Cu^{2+} or as Cu^{+} under aerobic or anaerobic conditions, and *Syn*Ftn. These data were unexpected because Cu^{2+} binding has previously been detected for ferritins not implicated in copper stress response (14, 15). Therefore, it seems that the function of *Syn*Ftn under copper stress is not associated with the direct sequestration of copper.

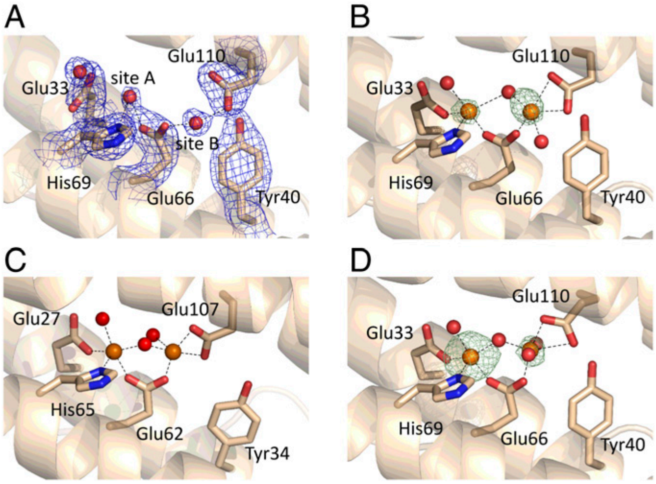

Fig. 1. Comparison of the ferroxidase centers of *Syn*Ftn and human H-chain ferritin (HuHF). (*A*) The apo ferroxidase center of *Syn*Ftn at pH 6.5, PDB entry 5OUW (56), with the double-difference Fourier ($2mF_o–DF_c$) map in the vicinity of the iron binding sites contoured at 1.1σ represented as a blue mesh. Metal binding sites, labeled A and B, are occupied by water molecules. Site A is predicted to have higher affinity for iron than site B. (*B*) The ferroxidase center of *Syn*Ftn following a 2-min soak in a solution containing 5 mM Fe^{2+} at pH 6.5 with the anomalous difference map contoured at 8σ in the same region (PDB entry 6GKC; ref. 57). (*C*) The ferroxidase center of HuHF following a 30-min soak in aerobic Fe^{2+}-containing solution at pH 8 from PDB entry 4YKH (19). (*D*) As in *B*, other than the soaking time for the crystal was increased to 20 min and the anomalous difference map contoured at 10σ (PDB entry 6GKA; ref. 58). Iron and water oxygen atoms are shown as orange and red spheres, respectively. Side chains of selected residues are shown in stick representation. The dashed lines in *B* and *D* indicate metal ligand bonds to the higher occupancy, Fe_A, and lower occupancy, Fe_B, iron sites. We note that the Fe–O–Fe core of the HuHF structure is more similar to the 20-min soak structure of *Syn*Ftn than it is to the 2-min soak structure, in which Fe_B and the bridging O(H) are in different positions, consistent with the assignment of the 2-min soak structure to a mixed-valent form.

Crystals of *Syn*Ftn that were soaked under aerobic conditions in Fe^{2+} for either 2 min (Fig. 1*B*) or 20 min (Fig. 1*D*) revealed two additional areas of electron density at the ferroxidase center and a third in the threefold channel that penetrates the protein coat, all modeled as iron. Rearrangement of the side chain of Glu33, a ligand to one of the metal ions, was apparent in both iron-soaked structures, as was bridging electron density between the metal centers. There was no evidence of electron density from a third metal bound at the ferroxidase center, and we conclude that site C is absent from *Syn*Ftn, as predicted from the sequence. As such, it is unique among characterized prokaryote ferritins, and in this sense the *Syn*Ftn ferroxidase center bears far greater resemblance to animal H-chain proteins (Fig. 1*C*). Thus, like other prokaryotic ferritins, *Syn*Ftn is composed solely of H-chain–like subunits lacking a carboxylate-rich patch, but the catalytic center lacks the ligands for site C, the defining feature of other prokaryotic ferritins, defying categorization according to the scheme described above.

Aerobic incubation with Fe^{2+} resulted in a color change, expected to be due to a diferric form of the ferroxidase center as it is in other ferritins. However, the Fe–Fe distance in the 2-min soak structure (3.90 Å; Fig. 1*B* and *SI Appendix*, Tables S1–S3) was far longer than in diferric ferroxidase center structures (15). Increasing the soaking time to 20 min resulted in a contraction of the Fe–Fe distance to 3.46 Å (Fig. 1*D* and *SI Appendix*, Tables S1–S3). Concomitant with the contraction in Fe–Fe distance was an increase in the angle formed by these two iron ions and the bridging density, from 113.0 to 116.7°. Both of these changes are consistent with those observed for oxidation of a hydroxy-bridged mixed-valent Fe^{2+}/Fe^{3+} model complex to an oxo-bridged di-Fe^{3+} state (16), suggesting that the unexpectedly long Fe–Fe

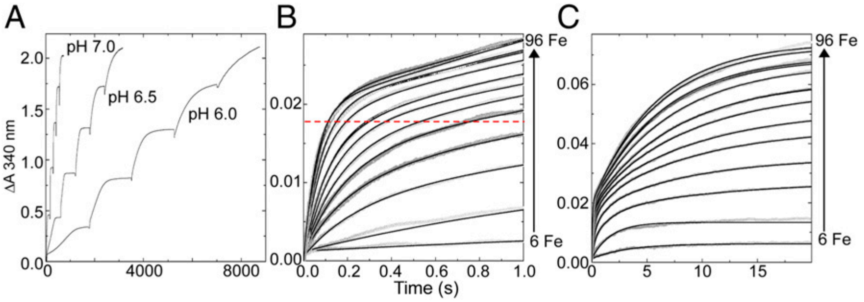

Fig. 2. Absorbance monitored iron–O_2 reactivity of *Syn*Ftn. (*A*) pH dependence of the rate of mineral core formation on consecutive addition of aliquots of 400 Fe^{2+} per *Syn*Ftn up to the maximum core capacity of 2,000 Fe/*Syn*Ftn. (*B*) Iron oxidation during the first second following mixing of increasing ratios of Fe^{2+} to 0.5 μM *Syn*Ftn at pH 6.5. Data shown in gray, black traces represent progress curves calculated from Eq. **1** using the values of ΔA_{340} and *k* specified in *SI Appendix*, Fig. S2. The broken red line indicates the predicted increase in absorbance at 340 nm for oxidation of 24 Fe^{2+}/Ftn. (*C*) Equivalent traces to *B* over the first 20 s following mixing of increasing ratios of Fe^{2+} to 0.5 μM *Syn*Ftn at pH 6.5 showing the second, slower phase of oxidation.

distance in the 2-min soak results from the formation of a hydroxy-bridged mixed-valent ferroxidase center (MVFC) that is subsequently oxidized to the oxo-bridged di-Fe^{3+} form upon prolonged exposure to O_2.

Formation of a Mixed Valent (Fe^{2+}/Fe^{3+}) Diiron Center in *Syn*Ftn. The kinetics of the initial iron–O_2 reaction at the catalytic sites following addition of Fe^{2+} to apo *Syn*Ftn were monitored using stopped-flow absorbance at a single wavelength of 340 nm (Fig. 2 *B* and *C*). The observed dependence on the stoichiometry of Fe^{2+} to protein was complex (*Materials and Methods* and *SI Appendix*, Fig. S2 *A*–*C*). Rapid oxidation of Fe^{2+} ($t_{1/2}$ < 200 ms) was observed only at loadings ≥18 Fe^{2+}/*Syn*Ftn. *Syn*Ftn variants E33A and E110A, in which iron-binding residues from each ferroxidase center site were individually substituted, were virtually inactive (*SI Appendix*, Fig. S2*D*). Together, and in the absence of cooperative binding of Fe^{2+} at ferroxidase centers, these observations suggest that optimum catalytic activity requires binding of iron to both ferroxidase center sites, as in other ferritins. The amplitude of the absorbance change associated with rapid oxidation increased linearly with iron loading up to 48 Fe^{2+}/*Syn*Ftn, sufficient to saturate all available ferroxidase center sites. While the rate of rapid oxidation continued to increase at greater iron loadings, the amplitude of the absorbance change associated with this phase saturated at approximately one-half that expected from equivalent measurements of other ferritins (*SI Appendix*, Fig. S2*A*) (17–19). A slow phase of Fe^{2+} oxidation was also apparent, and, at iron loadings sufficient to saturate the ferroxidase center sites, the sum of the amplitudes of the absorbance increases associated with the rapid and slow phases accounted for the oxidation of all added Fe^{2+}. At low iron loadings (<18 Fe^{2+}/Ftn), oxidation was dominated by a kinetically distinct phase characterized by an apparent rate constant intermediate between those of the rapid and slow processes (*SI Appendix*, Fig. S2 *A* and *C*). The amplitude of this phase decreased with increasing iron loading such that it was only a minor component when the iron loading was ≥18 Fe^{2+}/Ftn, and not observed at all at ≥48 Fe^{2+}/Ftn. Importantly, spectrokinetic measurements performed under similar conditions showed no evidence of formation of a DFP intermediate during rapid iron oxidation (*SI Appendix*, Fig. S2*E*), suggesting a mechanism of iron oxidation distinct from all previously reported ferritins.

Electron paramagnetic resonance (EPR) measurements of samples frozen 12 s after aerobic addition of Fe^{2+} to *Syn*Ftn resulted in detection of a paramagnetic species with g values all below 2.0 (Fig. 3*A*). The signal was remarkably similar to those observed previously upon partial reduction of the di-Fe^{3+} sites of *Pyrococcus furiosus* Ftn (20), human H-chain ferritin (21), and model diiron complexes (22). It was therefore assigned as arising from the formation of a Fe^{2+}/Fe^{3+} MVFC. Importantly, none of the ferritins mentioned above give rise to a MVFC directly upon reaction with O_2; they all form a Fe^{3+}/Fe^{3+} species that can be subsequently partially reduced to the MVFC. Direct MVFC formation in *Syn*Ftn was observed even for iron loadings (12 Fe^{2+}/Ftn) below that at which rapid oxidation was detected by stopped-flow absorbance. However, the intensity increased markedly at loadings ≥24 Fe^{2+}/*Syn*Ftn (1 Fe^{2+} per ferroxidase center) (Fig. 3*B*), consistent with the requirement for simultaneous occupancy of both iron binding sites.

The kinetics of MVFC formation were followed by rapid freeze–quench (RFQ) EPR. The intensity maximized ∼1 s after addition of saturating Fe^{2+}, at which point it was present on ∼70% of protein monomers (i.e., ∼17 MVFCs per 24-mer), before decaying away over the next 10 s (Fig. 3 *C* and *D*). Simulation of the MVFC envelope (Fig. 3*A* and Table 1) could be achieved only by assuming two overlapping components with g values at 1.943, 1.800, and 1.760 (major species, 80% of signal) and 1.955, 1.870, and 1.790 (minor species, 20% of signal), reminiscent of the result of one-electron reduction of the diferric iron–oxo center of *P. furiosus* Ftn (20). The major species accounted for 56% of ferroxidase centers at peak intensity, and the minor species, a further 14%. Samples for RFQ EPR could not be prepared under identical conditions to stopped-flow absorbance measurements (*Materials and Methods*). However, the time dependence of the intensity of the MVFC signal was consistent with formation of this species during the rapid phase of iron oxidation detected using stopped flow, and subsequent decay during the slow phase (Fig. 3*D*).

The formation of a MVFC intermediate on the pathway to mineral core formation explains not only the unusually large Fe–Fe distance in crystals soaked aerobically in Fe^{2+} for 2 min, but also the observation that only 50% of the Fe^{2+} bound at ferroxidase centers is oxidized in the initial rapid phase of activity.

The MVFC Forms and Decays Throughout Mineralization in *Syn*Ftn. Incubation of *Syn*Ftn with larger excess of Fe^{2+} over ferroxidase center sites led to greater longevity of the MVFC signal (*SI Appendix*, Fig. S3*B*), indicating that the intermediate is continually generated during turnover and that the ferroxidase center continues to function as the principal catalytic center following the initial reaction of Fe^{2+} and O_2. To investigate whether ferroxidase center activity can be regenerated, *Syn*Ftn was incubated with 400 Fe^{2+}/Ftn for 4 min (sufficient time for complete oxidation of all Fe^{2+}) and immediately exposed to a further 72 Fe^{2+}/Ftn. This sample exhibited ∼30% recovery of the rapid oxidation phase measured by stopped flow (with a rate constant indistinguishable from that for the apo-protein; *SI Appendix*, Fig. S3 *C* and *D*). The extent of this recovery increased when the incubation time between the initial and subsequent Fe^{2+} additions

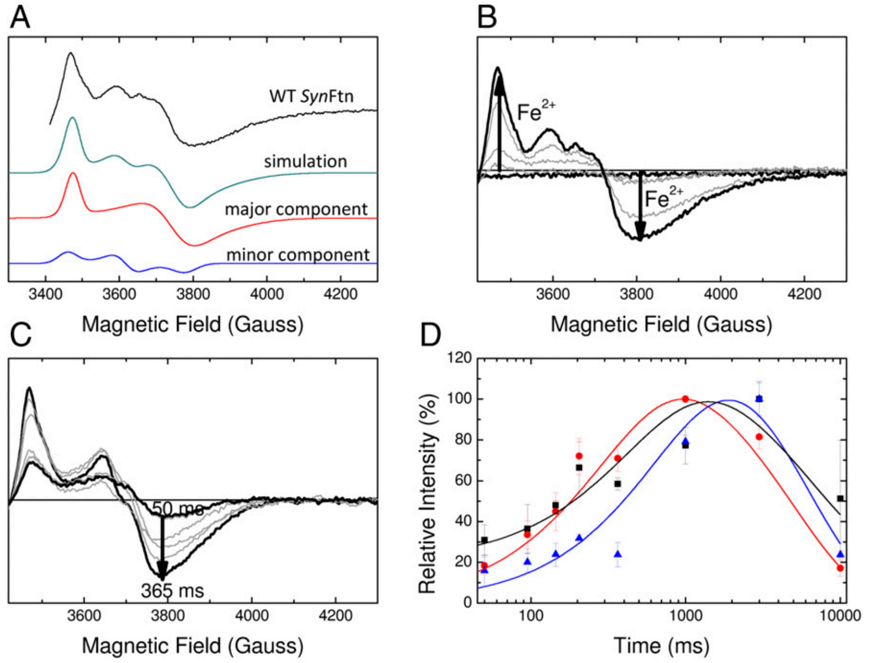

Fig. 3. EPR monitored iron–O_2 reactivity of *Syn*Ftn. (*A*) The EPR signal attributed to a mixed-valent (Fe^{2+}/Fe^{3+}) form of the ferroxidase center (MVFC) in *Syn*Ftn frozen 12 s after initiating iron oxidation (iron added at 80 Fe^{2+}/Ftn) and its modeling as a sum of two signals simulated with the parameters listed in Table 1. Experimental data are truncated to omit the region of overlap with the tyrosyl radical (Fig. 5). (*B*) Intensity of the MVFC signal at increasing iron loading in samples of 4.17 μM *Syn*Ftn in 100 mM Mes, pH 6.5, frozen 10 s after mixing. Response from the apo protein and protein loaded with 80 Fe^{2+} per Ftn are shown in black; intermediate loadings (12, 24, and 48 equivalents of Fe^{2+}) are shown in gray. (*C*) Increase in signal intensity in the high field region ($g < 2$) assigned to the MVFC in samples of 4.17 μM *Syn*Ftn frozen 50–365 ms after mixing with 72 equivalents of Fe^{2+}. Thick traces are the shortest (50 ms) and longest (365 ms) aging times shown, the latter corresponding to maximum signal intensity. Traces at intermediate freezing times are shown in gray. The EPR signal minimum at ∼3,800 G shifts in both sets of spectra, for iron load (*B*) and reaction time (*C*), due to increasing relative input of the "minor" MVFC component (*A*), which has a greater g_z value than the "major" one (Table 1). (*D*) Intensity plots showing the formation and decay of the MVFC (red circles), mononuclear Fe^{3+} (black squares), and tyrosyl radical (blue triangles) detected by low-temperature EPR spectroscopy over the first 10 s of iron oxidation (72 Fe^{2+}/Ftn) by *Syn*Ftn. Solid lines represent fits of the data, yielding apparent first-order rate constants of 3.0 s^{-1} (MVFC), 2.0 s^{-1} (Fe^{3+}), and 1.2 s^{-1} (Tyr radical) for the formation phase, and 0.2 s^{-1} (MVFC), 0.15 s^{-1} (Fe^{3+}), and 0.17 s^{-1} (Tyr radical) for the decay phase. Data for the MVFC can be compared with those for Fe^{2+} oxidation measured by stopped-flow absorbance at 10 °C (*SI Appendix*, Fig. S3*A*), for which apparent first-order rate constants of 8.3 s^{-1} (rapid phase) and 0.3 s^{-1} (slow phase) were obtained.

was increased, attaining 80% at 1 h, at which point the extent of recovery became invariant with increased incubation. Therefore, as with many other ferritins, the di-Fe^{3+} form of the ferroxidase center is unstable leading to translocation of Fe^{3+} into the central cavity and regeneration of the initial, rapid phase of Fe^{2+} oxidation.

O_2 Reduction by *Syn*Ftn. Reduction of O_2 by a single electron, derived from formation of the MVFC, would yield the superoxide radical anion. The EPR spectrum of *Syn*Ftn frozen at any point during turnover contained no features attributable to superoxide, nor was its presence detectable using the spin trap 5,5-dimethyl-1-pyrroline-*N*-oxide (DMPO) (*SI Appendix*, Fig. S4*A*). Superoxide may be transiently formed during the initial reaction of iron and O_2, but the detection of near-stoichiometric concentrations of MVFC in the EPR spectra demonstrates that it cannot remain bound here before the second, slower oxidation to the di-Fe^{3+} form. Together, these observations suggest that any superoxide produced upon MVFC formation is consumed before the oxidation of the catalytic site to the Fe^{3+}/Fe^{3+} form, indicating that the mechanism of MVFC formation is more complex than a simple one-electron reduction of O_2.

The stoichiometry of the iron/O_2 reaction, measured using an O_2 electrode, was found to be ∼2 Fe^{2+} per O_2 for the initial phase of iron oxidation (Fig. 4*A*), indicating that hydrogen peroxide is the final product of O_2 reduction. Indeed, peroxide ion was readily detected using the Amplex Red assay (Thermo Fisher), at close to the expected 2:1 ratio of Fe^{2+} to H_2O_2 (Table 2). An Fe^{2+}:O_2 ratio of 2:1 is reported for eukaryotic H-chain homopolymers, but this ratio gradually increases toward 4:1 during mineralization due to peroxide-mediated oxidation of Fe^{2+} at the growing mineral surface (23). No evidence for peroxide involvement in *Syn*Ftn-mediated Fe^{2+} oxidation was found: the di-Fe^{2+} form of the ferroxidase center did not react with exogenously added peroxide, and the Fe^{2+}:O_2 ratio remained at ∼2:1 even during mineralization (Fig. 4*B*).

Table 1. Principal g values and individual linewidths used in simulation (S = 1/2) of the two components of the EPR signal assigned to MVFC in *Syn*Ftn

Component	g_x	g_y	g_z	ΔH_x, G	ΔH_y, G	ΔH_z, G	Contribution, %
Wild-type MVFC major component	1.943	1.800	1.760	35	95	230	80
Wild-type MVFC minor component	1.955	1.870	1.790	50	56	63	20
Y40F MVFC major component	1.943	1.798	1.765	40	100	320	83
Y40F MVFC minor component	1.955	1.840	1.770	40	40	80	17

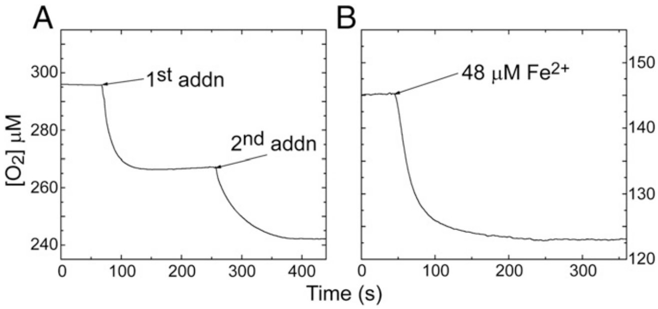

Fig. 4. O_2 consumption during Fe^{2+} oxidation by *Syn*Ftn. (*A*) Change in dissolved O_2 concentration following successive additions of 48 equivalents (48 μM) of Fe^{2+} to 1 μM apo *Syn*Ftn in 100 mM Mes, pH 6.5, at 20 °C. (*B*) As for *A*, but following addition of 48 equivalents of Fe^{2+} to 1 μM *Syn*Ftn containing a freshly prepared mineral core of 400 Fe^{3+}/SynFtn.

MVFC Formation Involves Cooperation Between Pairs of Ferroxidase Centers. The lack of evidence for superoxide formation, the ~2:1 Fe^{2+}:O_2 ratio, and stoichiometric formation of hydrogen peroxide raise the key question of how these result from the oxidation of a single Fe^{2+} at each ferroxidase center of *Syn*Ftn. The simplest explanation is that the ferroxidase centers function in pairs, each delivering a single electron to an O_2 molecule bound at only one of them. This proposal requires that O_2 reacts directly with a maximum of 50% of ferroxidase centers during each catalytic cycle, the remainder of the observed MVFCs being formed by electron transfer away from di-Fe^{2+} sites with no O_2 bound.

In addition to the MVFC, mononuclear high-spin Fe^{3+} was also detected by EPR, at g = 4.3 (*SI Appendix*, Fig. S4*B*), upon reaction of *Syn*Ftn with Fe^{2+} and O_2. Both species formed with similar rapid kinetics (Fig. 3*D*), and so the Fe^{3+} species is not a breakdown product of the fully oxidized ferroxidase center. As both E33A and E110A variants were inactive, it is apparent that, as for other ferritins, both ferroxidase center iron binding sites are required for catalytic activity (7, 24). Thus, it is highly unlikely that the mononuclear Fe^{3+} signal results from the reaction of Fe^{2+} and O_2 at singly occupied ferroxidase centers. Rather, we propose that electron transfer from ferroxidase centers singly occupied by Fe^{2+}, most likely at the predicted higher-affinity site (site A in Fig. 1*A*), results in mononuclear high-spin Fe^{3+} formation. Quantification by comparison with a high-spin Fe^{3+}-bound protein standard indicated that, at maximum intensity, high-spin Fe^{3+} was present on ~8% of *Syn*Ftn monomers (two high-spin Fe^{3+} per 24-mer). Therefore, overall EPR spin quantitation demonstrated that, during the initial, rapid reaction with O_2, a maximum of ~80% of ferroxidase centers are in a paramagnetic state, before quenching to antiferromagnetically coupled EPR-silent species during a subsequent slower phase.

A model in which pairs of ferroxidase centers cooperate for rapid formation of MVFC and hydrogen peroxide not only accounts for the simultaneous formation of MVFC and mononuclear Fe^{3+} (Fig. 3*D*), but is also consistent with the kinetic dependence of Fe^{2+} oxidation on the ratio of Fe^{2+}:*Syn*Ftn. At low iron (e.g., 12 Fe^{2+}/24-mer), the MVFC was still formed (Fig. 3*B*), but the rapid phase of Fe^{2+} oxidation was not observed because there was insufficient occupation of closely located pairs of ferroxidase centers for rapid electron transfer to occur.

The above model requires the presence of an electron transfer pathway between ferroxidase centers. Since it was first postulated for a diiron, O_2-activating protein (25), the transient oxidation of aromatic amino acid side chains has been accepted as a means of such electron transport across large distances in proteins without need for redox active cofactors (26). In addition to the MVFC and Fe^{3+} signals, EPR spectra revealed the presence of a signal that is characteristic of a tyrosyl radical (Fig. 5*A*) with an intensity that increased linearly with added Fe^{2+} at loadings up to 80/Ftn and maximized within the first second of reaction (Fig. 5 *B* and *C*). Quantification of this signal revealed that it is present on ~5% of monomers. Consequently, to assess the functional relevance, we sought to determine which of the six tyrosine residues in the *Syn*Ftn monomer hosts the radical.

Tyr40 Is Essential for Rapid MVFC Formation. An interferroxidase center electron transfer pathway would most likely involve Tyr40, a residue that is ~4 Å away from the Fe_B site, is conserved among all ferritins containing a catalytic diiron center (*SI Appendix*, Fig. S1*B*), and is reported to be the site of radical formation in several (12, 27, 28). The EPR spectrum of the radical species formed by *Syn*Ftn was simulated (Fig. 5*A*) using the tyrosyl radical spectra simulation algorithm (TRSSA) (29). The set of hyperfine splitting parameters used in the simulation suggested a specific tyrosyl side-chain conformation that was in good agreement with that of Tyr40 in the structures of *Syn*Ftn reported here (*SI Appendix*, Tables S4 and S5). Consequently, the structure, activity, and spectroscopic properties of a Y40F variant of *Syn*Ftn, in which this residue is replaced by the nonoxidizable analog phenylalanine, were investigated.

The crystal structure of this variant (PDB entry 5OUZ; ref. 30) revealed no significant changes beyond the substituted side chain (*SI Appendix*, Fig. S5 *A* and *B*). Iron soak experiments revealed only one iron bound at the ferroxidase center, at the high-affinity site A (PDB entry 6GKB; ref. 31). Rapid oxidation of Fe^{2+} was completely abolished in Y40F *Syn*Ftn (Fig. 6 *A*–*C* and *SI Appendix*, Fig. S5 *C* and *D*). However, binding of iron to both ferroxidase center sites was confirmed by detection of the characteristic MVFC EPR signal (Fig. 6*D*), although the MVFC formed at a rate much slower than in the wild-type protein (Fig. 6 *E* and *F*), consistent with the kinetics of Fe^{2+} oxidation deduced from the stopped-flow data. As with the wild-type protein, two species were required to simulate the observed signal (Fig. 6*D* and Table 1). Quantification revealed a maximal intensity corresponding to 60% of the subunit concentration (i.e., 14 MVFC per 24-mer) 3 s after addition of Fe^{2+}. Furthermore, EPR spectra of Y40F *Syn*Ftn showed no evidence of tyrosyl radical formation at any point during O_2-driven Fe^{2+} oxidation. However,

Table 2. **Activity, O_2 reduction, and peroxide production by *Syn*Ftn and variants**

Protein	Mineralization rate, μM·min^{-1}	Fe:O_2 stoichiometry		H_2O_2 detected, % stoichiometric yield		
		Ferroxidation*	Mineralization	24 Fe^{2+}/Ftn	48 Fe^{2+}/Ftn	72 Fe^{2+}/Ftn
Wild type	46	1.9 ± 0.1	2.0 ± 0.1	105 ± 3	70 ± 2	53 ± 2
Y40F	33	2.0 ± 0.1	2.4 ± 0.1	47 ± 2	28 ± 2	25 ± 2
E33A	0.5†	—	—	—	—	—
E110A	0.7	—	—	—	—	—

*The uncertainty in listed values was estimated from the SE from three independent measurements.

†Low activity of variants E33A and E110A rendered measurement of O_2 reduction and H_2O_2 production impractical.

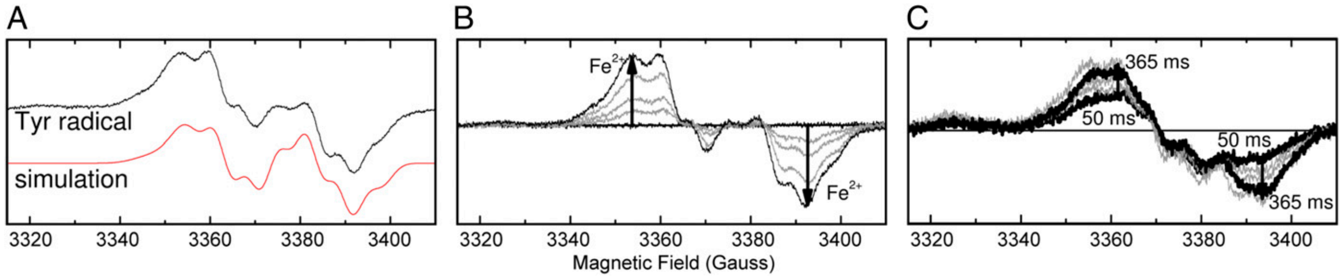

Fig. 5. The transient tyrosyl radical of *Syn*Ftn. (*A*) EPR signal due to a tyrosyl radical in *Syn*Ftn frozen 12 s after initiating iron oxidation (iron added at 80 Fe^{2+}/Ftn). The simulation parameters are reported in *SI Appendix*, Table S4. (*B*) Intensity of the tyrosyl radical signal at increasing iron loading in samples of 4.17 μM *Syn*Ftn in 100 mM Mes, pH 6.5, frozen 10 s after mixing. Response from the apo protein and protein loaded with 80 Fe^{2+} per Ftn are shown in black, and intermediate loadings (12, 24, and 48 equivalents of Fe^{2+}) are shown in gray. (*C*) Increase in signal intensity due to the radical at approximately g = 2 in samples of 4.17 μM *Syn*Ftn frozen 50–365 ms after mixing with 72 equivalents of Fe^{2+}. Thick traces are the shortest (50 ms) and longest (365 ms) aging times shown. Traces at intermediate freezing times are shown in gray.

absorbance measurements over a longer time period following addition of 400 Fe^{2+} per protein showed that mineralization proceeded at a rate similar to that of the wild-type protein (*SI Appendix*, Fig. S2*D*). For protein concentrations of 0.5 μM, all Fe^{2+} oxidation in Y40F *Syn*Ftn proceeded at the rate observed for the slow oxidation of the MVFC to the diferric form for the wild-type protein, suggesting that this process is the rate-limiting step for core formation under these conditions. This rate is unaffected by substitution of Tyr40, the site of radical formation essential for rapid oxidation of Fe^{2+}, and so we conclude that initial reaction of O_2 with di-Fe^{2+} *Syn*Ftn ferroxidase centers produces a species capable of oxidizing a Tyr residue, but the subsequent, slower oxidation of the MVFC does not.

The observed Fe:O_2 reaction stoichiometry for Y40F *Syn*Ftn was slightly greater than that for the wild-type protein (Table 2 and *SI Appendix*, Fig. S5*E*). This increase is most likely due to impaired ferroxidase center function; because Fe^{2+} persists in solution for longer it is susceptible to oxidation by peroxide released during the reaction cycle, a hypothesis supported by the detection of hydroxyl radical in spin trapping experiments (*SI Appendix*, Fig. S4*A*) and low levels of peroxyl radical (*SI Appendix*, Fig. S4*B*) in EPR measurements at cryogenic temperatures conducted with this variant.

Discussion

The prokaryotic ferritin *Syn*Ftn contains a catalytic ferroxidase center that more closely resembles those of eukaryotic H-chain ferritins than ferritins isolated from other prokaryotes. An H-chain–type mineralization mechanism with direct formation of a DFP intermediate was therefore anticipated, but instead *Syn*Ftn produced a mixed-valent Fe^{2+}/Fe^{3+} species upon reaction with Fe^{2+} and O_2. Mixed-valent diiron centers are known, for example in hemerythrins (32), purple acid phosphatases (33), rubrerythrins (34), ribonucleotide reductase (35), soluble methane monooxygenase (36), and the HD-domain protein superfamily members *myo*-inositol oxygenase (MIOX) (37) and PhnZ (38). However, in all cases other than MIOX, these mixed-valent centers cannot be formed by reaction of the di-Fe^{2+} site with O_2 and are generally accessed by reduction of the di-Fe^{3+} state.

Many carboxylate-bridged diiron proteins are characterized by a four α-helical bundle motif that coordinates the diiron center via a carboxylate-rich ligand set. This group includes ribonucleotide reductase, methane monooxygenase, plant fatty acyl-ACP desaturase, toluene/*o*-xylene monooxygenase, toluene 4-monooxygenase, and members of the ferritin family (39–41), and all activate O_2 to form a di-Fe^{3+}-peroxo intermediate. MIOX is distinct from this group in that its diiron site is housed in an HD domain, where five helices contribute a histidine-rich coordination environment. The catalytically active form of MIOX is the mixed-valent Fe^{2+}/Fe^{3+} state, which is formed in an activating step before further reaction with O_2 generating a highly oxidizing di-Fe^{3+}–superoxo complex that enables the enzyme to cleave a C–H bond. The di-Fe^{2+} state of MIOX can react with O_2 to form the Fe^{2+}/Fe^{3+} state but only either under limiting O_2 or in the presence of an exogenous reducing agent (42). Under other conditions, the oxidation to a di-Fe^{3+} state common to all other carboxylate-bridged diiron oxygenases occurs. Therefore, the formation of a MVFC in *Syn*Ftn is surprising given that it occurs regardless of the level of O_2 excess and in the absence of a reductant, and that the ligand set of the Fe_A and Fe_B sites of *Syn*Ftn are identical to those of the iron ions in animal ferritins, in which the first detectable intermediates are DFP species. Also, ferritins have no obvious need of highly oxidizing intermediates during their reaction cycles leading to mineral formation, and further reaction of the MVFC of *Syn*Ftn forms only a di-Fe^{3+} state similar to that produced in a concerted step by other ferritins.

The product of oxygen reduction in the activating step of MIOX has not been determined, but, given the absence of any potential electron donors other than the diiron site, presumably superoxide is formed. EPR spectra yielded no evidence of superoxide production by *Syn*Ftn, while almost stoichiometric levels of peroxide were detected. The peroxide produced does not react further with the mixed-valent center, nor with Fe^{2+} in the cavity, another unexpected feature given the propensity of peroxide to oxidize Fe^{2+}. In further contrast to MIOX, three paramagnetic species were detected by EPR for *Syn*Ftn, all forming too rapidly to be associated with the second, slower phase of iron oxidation detected by stopped-flow absorbance. The time dependence of the *Syn*Ftn MVFC EPR signal intensity suggests that it may form more slowly than iron is oxidized in the initial rapid phase. This discrepancy is most likely accounted for by the slightly lower temperature at which RFQ mixing experiments were conducted, but an alternative explanation is that the MVFC is formed by reduction of a di-Fe^{3+} intermediate. This possibility is unlikely because (*i*) no spectroscopic evidence for a ferric-peroxo species was apparent; (*ii*) it is unclear how a Fe^{3+}/Fe^{3+} diiron site could be sufficiently oxidizing to generate a Tyr radical (such a reaction is without precedent); (*iii*) there was no evidence for two phases in the initial part of the stopped-flow data; (*iv*) the X-ray crystal structures of mixed-valent and di-Fe^{3+} forms of the protein were obtained by incubation of apo-*Syn*Ftn crystals in aerobic Fe^{2+} solution for increasing time periods, reflecting the formation of the Fe^{2+}/Fe^{3+} form before the di-Fe^{3+} form; and (*v*) substitution of Tyr40 resulted in loss of rapid oxidation; the above alternative would be expected to result in unaffected oxidation to the di-Fe^{3+} form and its stabilization in the absence of the oxidizable Tyr.

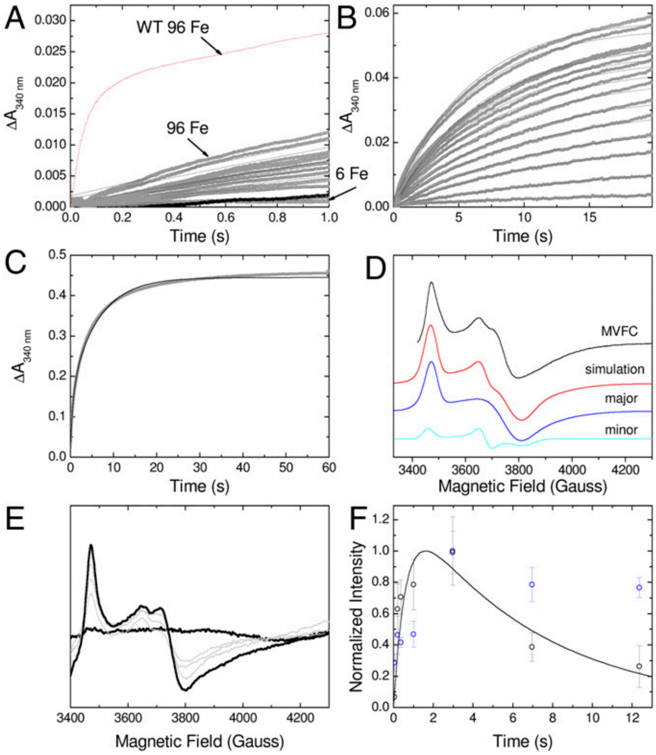

Fig. 6. Absorbance and EPR monitored iron–O_2 reactivity of the Y40F variant of *Syn*Ftn. (*A*) Increase in A_{340} over the first second following aerobic mixing of between 6 and 96 Fe^{2+} per *Syn*Ftn. Data in gray, black traces show the progress curves calculated from the parameters plotted in *SI Appendix*, Fig. S5 *C* and *D*. The red trace shows the response following addition of 96 Fe^{2+} to wild-type *Syn*Ftn for comparison. (*B*) Data as in *A* showing the response over the first 20 s following mixing. Over this time period, only a single exponential was required to fit the traces at all iron loadings and the apparent rate constants describing this process were in good agreement with those for the slow phase of oxidation observed in wild-type *Syn*Ftn. (*C*) A_{340} as a function of time following mixing of a solution of 4.17 μM Y40F *Syn*Ftn with 72 equivalents of Fe^{2+} at 20 °C. Data are shown as gray circles; black trace represents a biexponential function fitted through the data, described by apparent first-order rate constants of 1.5 and 0.16 s^{-1}. (*D*) Low-temperature EPR signal attributed to the formation of a mixed-valent (Fe^{2+}/Fe^{3+}) form of the ferroxidase center (MVFC) in Y40F *Syn*Ftn frozen 15 s after aerobic addition of 72 Fe^{2+} per *Syn*Ftn and its modeling as a sum of two EPR signals simulated with the parameters listed in Table 1. Experimental data are truncated to omit the region of overlap with intensity from the peroxyl ($ROO^•$) radicals observed in place of the tyrosyl radical of the wild-type protein (*SI Appendix*, Fig. S4*B*). (*E* and *F*) Time dependence of Y40F *Syn*Ftn EPR. (*E*) Increase in signal intensity in the high field region ($g < 2$) assigned to the MVFC in solutions equivalent to that in *C* frozen 50–2,965 ms after mixing with 72 equivalents of Fe^{2+}. The thick traces are the shortest (50 ms) and longest (2,965 ms) aging times shown, the latter corresponding to maximum signal intensity. Traces at intermediate freezing times are shown in gray. (*F*) Normalized intensity of observed EPR signals as a function of time after mixing of Y40F *Syn*Ftn and 72 equivalents of Fe^{2+}. Sample conditions were as in *E*. MVFC intensity is shown as black circles, and mononuclear Fe^{3+} as blue. The black trace shows the predicted kinetics of a species formed in a first-order reaction at the faster rate derived in *C* and consumed at the slower.

Thus, the data are consistent with the direct formation of the MVFC upon reaction with O_2 followed by a slower oxidation to the di-Fe^{3+} state. Variability in the integrated intensities of EPR signals between independent RFQ samples meant that it was unclear whether the MVFC, tyrosyl radical, and mononuclear ferric iron form at exactly the same rate. However, the data demonstrate unequivocally that these species are formed during the initial rapid phase of Fe^{2+} oxidation and are not formed sequentially.

Quantification of the EPR signals showed that only the MVFC forms in sufficient yield to be a reasonable candidate for the ultimate source of reducing equivalents for O_2. Oxidation of only one of two Fe^{2+} ions at each diiron site, together with an overall Fe^{2+}:O_2 ratio of 2:1 and peroxide as the product of O_2 reduction, indicates that pairs of ferroxidase centers (separated by ∼24.5 Å) function together to deliver two electrons to a shared O_2 substrate. Therefore, the data point to the existence of a long-range electron transfer pathway between ferroxidase centers, and the transient formation of a radical on the strictly conserved residue Tyr40 is consistent with such a pathway (Fig. 7). Here, the Tyr40 radical is formed simultaneously with the MVFC and almost immediately quenched by oxidation of Fe^{2+} at the second, remote ferroxidase center, generating a second MVFC or a mononuclear Fe^{3+}, depending on the occupancy, the Tyr radical itself only being detected if the partner iron binding site is vacant. While the MVFC is the intermediate that drives mineralization, Tyr40 is essential for rapid oxidation, presumably because intercenter electron transfer is inhibited in the absence of an oxidizable sidechain close to the ferroxidase center. While oxidation of a di-Fe^{2+} center to the Fe^{2+}/Fe^{3+} state and intersubunit electron transfer mediated by oxidation of aromatic amino acids have both been previously reported, the occurrence of both of these phenomena simultaneously to facilitate reduction of a shared O_2 substrate represents chemistry not previously identified among the widespread family of carboxylate-bridged diiron oxygenases.

A key question arising from this work is why this unique mechanism has evolved in this ferritin. Recalling that *Syn*Ftn is up-regulated in response to elevated copper levels may provide an answer. Copper toxicity is known to be mediated through

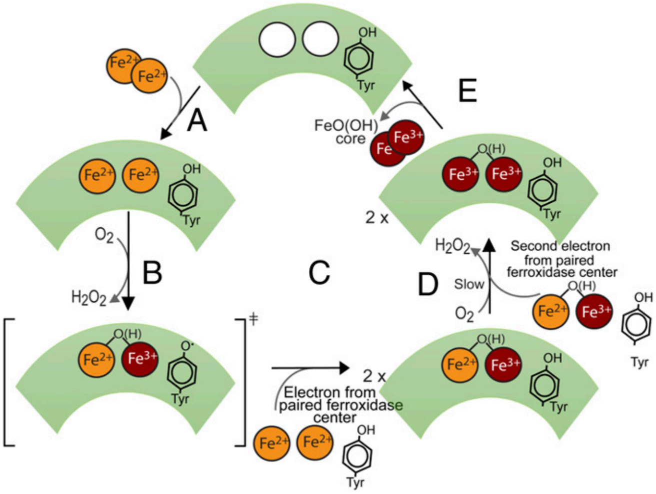

Fig. 7. Proposed catalytic cycle of *Syn*Ftn. (*A*) Apo ferroxidase center binds two Fe^{2+} ions from solution. (*B*) Two-electron reduction of O_2 to hydrogen peroxide leads to oxidation of a single Fe^{2+} ion, thus yielding the MVFC, and a radical on Tyr40. (*C*) The Tyr radical is transient and only observed in the subset of subunits where the partner subunit's ferroxidase center is unoccupied. In the remainder, rapid electron transfer from Fe^{2+}/Fe^{2+} or monomeric Fe^{2+} bound at a second ferroxidase center results in quenching of the radical. (*D*) Slow reaction of the MVFC with a second molecule of O_2, accompanied by transfer of a second electron from the paired ferroxidase center, results in formation of the unstable bridged diferric center observed in other ferritins and a second molecule of hydrogen peroxide. The kinetics of this process was unaltered in a Y40F variant, suggesting that Tyr40 is not required for transfer of the second electron. (*E*) Hydration and translocation of oxidized iron from the ferroxidase center to the internal cavity results in formation of mineral core and regeneration of apo ferroxidase centers. Overall, four ferroxidase center-bound Fe^{2+} ions are oxidized, reducing two molecules of O_2 to H_2O_2, accounting for the observed 2:1 stoichiometry.

redox stress and by the displacement of native metals from protein sites, particularly iron–sulfur cluster proteins (43). Under such circumstances, the organism would have an urgent need to rapidly remove free iron to prevent it from engaging in Fenton chemistry. Thus, the extremely rapid Fe^{2+} oxidation observed in *Syn*Ftn would serve to detoxify excess iron rapidly. Other ferritins achieve similar rates via oxidation of both Fe^{2+} ions, and so the requirement to suppress Fenton chemistry alone cannot account for the mechanism reported here. Of further potential importance is that, in contrast to the DFP intermediate generated by H-chain ferritins, the MVFC of *Syn*Ftn contains a single unpaired electron and as such would generate closed shell molecules following single-electron oxidation/reduction events with the reactive oxygen species superoxide radical and hydroxyl radical, of which both are generated under conditions of oxidative stress. Such quenching of toxic radicals may provide an additional mechanism of protection against oxidative stress.

Ferritins in general do not appear to be particularly widely distributed in cyanobacteria. Nevertheless, multiple sequence alignments of annotated ferritins from available cyanobacterial genomes (Dataset S1) revealed >100 homologs of *Syn*Ftn (with no site C), which occur almost exclusively in the marine picocyanobacteria (*Synechococcus* and *Prochlorooccus*). Furthermore, while the more standard prokaryotic ferritin (containing a site C) is found in a genetically more diverse set of cyanobacteria, it is also much less common than *Syn*Ftn (only 55 homologs found in the genomes surveyed). For example, a few species of *Prochlorococcus*, such as *Prochlorococcus* sp. strain MIT9313 and MIT9303, have both standard and *Syn*Ftn types, but the majority of *Prochlorococcus* have only one ferritin, and it is almost always a *Syn*Ftn (Dataset S1). *Syn*Ftn homologs appear to occur almost exclusively in cyanobacteria (we found only one example in other bacteria), suggesting that they fulfill a detoxification function that is somehow specialized for (marine) cyanobacteria. Furthermore, the prevalence of *Syn*Ftn in *Prochlorococcus*, a group known for their stringent genome streamlining (44), is indicative of the importance of this gene to fitness in picocyanobacteria.

Finally, a proposal that all ferritins mineralize iron via a common, "universal" mechanism (45) has gained significant exposure in recent times. The data presented here show unequivocally that *Syn*Ftn utilizes a mechanism distinct from those of all previously characterized ferritins, demonstrating that a single mechanism that describes all ferritins does not exist. Rather, the data provide further evidence for mechanistic diversity among members of this superfamily (6), and the important questions now focus on the reasons for it. *Syn*Ftn exhibits unique activity despite the ligands coordinating the diiron catalytic center being identical to those of other ferritins (Fig. 1 and *SI Appendix*, Fig. S1*B*). The substitution of several near ferroxidase center residues that are conserved in other ferritins may be the source of this difference (*SI Appendix*, Fig. S6), and a major challenge now is to elucidate the control of DFP versus MVFC reactivity exerted by such factors.

Materials and Methods

Protein Overexpression and Purification. Sync_1539 was amplified from CC9311 genomic DNA (primers CGGAATTCCATGGCTACCGACGTTGCTC and CCCCTCGAGGGTCAACCTCGCTGCGTTTGAC), resulting in a 569-bp product with EcoRI and AvaI cleavage sites on either end. Following purification and digestion with EcoRI and AvaI, PCR product was ligated into digested pET21b plasmid (Novagen) and used to transform One Shot TOP10 electrocompetent *E. coli* cells (Invitrogen) according to the manufacturer's specifications. Transformed cells were plated on LB plates containing 50 μg·mL^{-1} kanamycin and incubated overnight at 37 °C; colonies were picked into LB containing 50 μg·mL^{-1} kanamycin; and cultures were incubated at 37 °C overnight. Plasmid was purified from cultures using a Qiagen miniprep kit (Qiagen) and plasmid insert verified with Sanger sequencing. Plasmids for variants Y40F, E33A, and E110A cloned into pET21a (Novagen) were purchased from Genscript. The encoded proteins were overexpressed in *E. coli* strain BL21(DE3) (Promega). Cultures were grown in LB containing 100 μg·mL^{-1} ampicillin at 37 °C, 200 rpm shaking to OD_{600} of 0.6–0.8. Overexpression was induced by addition of isopropyl β-D-1 thiogalactopyranoside (20 μM), and cultures were grown for a further 3 h at 37 °C, 200 rpm shaking before harvesting by centrifugation. Cells were resuspended in 20 mM Hepes, pH 7.8, 100 mM KCl, 0.1 mM EDTA (buffer A) and disrupted by sonication, and debris was removed by centrifugation at 40,000 × *g* for 45 min. Thermally unstable proteins were precipitated from the supernatant by heating to 65 °C for 15 min and removed by centrifugation as before. Protein was precipitated from the supernatant via the addition of ammonium sulfate to a concentration of 0.55 g·mL^{-1}. The precipitate was solubilized in the minimum volume of buffer A and dialyzed against 1 L of identical buffer for 12 h. Contaminating proteins were removed by size-exclusion chromatography (HiPrep 26/60 Sephacryl S-300HR; GE Healthcare) and contaminating DNA by anion exchange chromatography (HiTrap Q FF; GE Healthcare). For the latter, protein solutions were loaded in buffer A and eluted by stepping to 50% buffer B (20 mM Hepes, pH 7.8, 100 mM KCl, 1.0 M NaCl, 0.1 mM EDTA). Protein as isolated contained small quantities of iron that was removed as previously described (5) before exchanging into 100 mM Mes, pH 6.5, by centrifugation over a 10-kDa molecular-weight cutoff cellulose membrane (Millipore). Sample purity was assessed using SDS/PAGE, and proteins were judged to be free of DNA contamination once the ratio of absorbance at 277 nm (wild type) or 276 nm (Y40F) and 260 nm reached 1.5.

Gel Filtration and Native PAGE of *Syn*Ftn. The association state of purified *Syn*Ftn was assessed by loading 0.5 mL of 25 μM protein onto a HiPrep 26/60 Sephacryl S-200HR size-exclusion column equilibrated with 100 mM Mes, pH 6.5. Column calibration under identical buffer conditions using protein standards of known molecular weight (Sigma) indicated a void volume of 106 mL and the expected dependence of elution volume on the logarithm of molecular weight. Assembly of *Syn*Ftn was also analyzed by native PAGE. Samples were loaded onto 6% (vol/vol) polyacrylamide gels containing 60 mM Hepes and 40 mM imidazole (pH 7.2). Gels were conditioned by running in 60 mM Hepes and 40 mM imidazole at a current of 10 mA for 1 h. Samples were then loaded in buffer containing 10% (vol/vol) glycerol, and the gel was run for a further 2 h with a limiting current of 5 mA.

Crystallization and Structure Determination. Protein (10 mg·mL^{-1}) exchanged into 20 mM Mes, pH 6.5, in 2-μL drops was mixed with an equal volume of well solution (0.1 M sodium acetate, 2.0 M NaCl, pH 4.6) and equilibrated in sitting drops by vapor diffusion against 200 μL of the same well solution. Crystals of bipyramidal morphology appeared within 24 h and grew to optimum size (100–150 μm) in ∼1 wk. Apo crystals were transferred to cryoprotectant comprising the well solution with pH adjusted to 6.5 containing 30% (vol/vol) glycerol before flash freezing in liquid nitrogen. Iron-containing crystals were prepared by soaking for either 2 or 20 min in well solution containing 5 mM Fe^{2+} ions at pH 6.5. Crystals were then cryoprotected and frozen as above but using a solution containing 5 mM Fe^{2+} in addition to 30% (vol/vol) glycerol. Diffraction data were collected on beamline i04 of the Diamond Light Source except for the 20 min Fe^{2+} soak of wild-type *Syn*Ftn, which was collected on beamline i03. The wavelength used was 0.9795 Å in all cases. To reduce the likelihood of photoreduction of metal centers in iron-containing samples, exposure to X-rays was minimized subject to the requirement that the resulting diffraction datasets should be at least 95% complete and have a multiplicity of no less than 3.0 in the highest resolution bin. Additional, highly redundant anomalous scattering data were collected from crystals of similarly treated iron-containing crystals of wild-type and Y40F *Syn*Ftn at wavelengths corresponding to the peak of the iron K-edge (around 1.7399 Å). All data were indexed and processed using XDS and Aimless as part of the automatic xia2 pipeline (46). Reprocessing was carried out as necessary using Aimless (47) as part of the CCP4 program suite (48). Statistics are summarized in *SI Appendix*, Table S1 for X-ray data used for structure solution and refinement and in *SI Appendix*, Table S2 for data used for calculation of Bijvoet-difference Fourier (anomalous-scattering-density) maps.

Structure solution was performed by molecular replacement using phenix.phaser MR (49) with the 2.05-Å resolution structure of *E. coli* FtnA, PBD entry 1EUM (50), as the search model. In all cases, the asymmetric unit contained a single copy of the protein monomer. Placement of metal ions was confirmed by reference to Bijvoet-difference Fourier maps calculated from anomalous scattering data (*SI Appendix*, Table S2). Model refinement employed iterative cycles using phenix.refine (50) and manual correction using COOT (51). No metal coordination restraints were applied to metal sites during refinement of iron-containing structures. Anisotropic temperature factor refinement was employed for all metal ions, and their occupancies were manually adjusted to ensure that the average B factor of the metal fell within ±14% of the B factors of atoms of their environment (52). The coordination geometry of metal binding sites was analyzed after refinement using the CheckMyMetal web server (53). Statistics relating to the metal binding sites in the refined structures can be found in *SI Appendix*, Table S3. Atomic coordinates and structure factors have been deposited in the Protein Data Bank, www.wwpdb.org (PDB ID codes 5OUW, 6GKC, 6GKA, 5OUZ, and 6GKB).

Kinetic Analysis of Iron Oxidation and Mineralization by *Syn*Ftn. Rates of iron oxidation were deduced from the rate of increase in A_{340} due to the resulting ferric-oxo species, be they iron bound at the ferroxidase center or in the mineral core. Typical assays employed 0.5 μM *Syn*Ftn in 100 mM Mes, pH 6.5, at 25 °C. Aerobic oxidation of ferroxidase center-bound Fe^{2+} following addition to apo *Syn*Ftn was complete in ~20 s. Accordingly, the kinetics of this process was monitored using stopped-flow absorbance spectroscopy. The 1.0 μM protein was mixed with an equal volume of Fe^{2+} of the appropriate concentration in 1 mM HCl using an Applied Photophysics Bio-Sequential DX.17MV spectrophotometer with a 1-cm pathlength observation cell. The time dependences of A_{340} increase were fitted to the sum of up to three exponential processes, encompassing rapid (r), intermediate (i), and slow (s) components, using OriginPro 8 (OriginLab):

$$\Delta A_{340}(t) = \Delta A_{340}^{(tot)} - \Delta A_{340}^{r} e^{-k_r t} - \Delta A_{340}^{i} e^{-k_i t} - \Delta A_{340}^{s} e^{-k_s t}. \quad [1]$$

The extent to which oxidized iron vacates the ferroxidase centers of *Syn*Ftn was investigated by monitoring the regeneration of the rapid phase of iron oxidation associated with the apo protein. The 1 μM protein was incubated with 400 μM Fe^{2+} at 25 °C for periods of 4, 5, 6, or 60 min before mixing with an equal volume of 48 μM Fe^{2+} in 1 mM HCl. An equivalent sample was incubated at 25 °C for 60 min followed by a further 19 h at 4 °C. After reequilibration at 25 °C, the protein was mixed with an equal volume of 48 μM Fe^{2+} in 1 mM HCl as above. Data for comparison of iron oxidation kinetics to the time dependence of EPR intensities were obtained by mixing 8.33 μM *Syn*Ftn in 100 mM Mes, pH 6.5, with equal volumes of 0.6 mM Fe^{2+} in 1 mM HCl, giving a final concentration of 4.17 μM *Syn*Ftn (100 μM in monomeric units) with an iron loading of 3.0 Fe^{2+} per monomer.

Attempts to detect formation and decay of a DFP intermediate during *Syn*Ftn-catalyzed iron oxidation by monitoring at single wavelengths between 550 and 650 nm were inconclusive. Therefore, a SX20 stopped-flow spectrophotometer (Applied Photophysics) equipped with a diode-array multiwavelength unit photomultiplier was employed to record spectra over the wavelength range of 350–700 nm. SVD analysis of spectro-kinetic data acquired following mixing of 3 μM *Syn*Ftn in 100 mM Mes, pH 6.5, with 0.5, 1.0, 2.0, or 2.5 Fe^{2+} (in 1 mM HCl) per ferroxidase center at 25 °C was carried out using ProK (Applied Photophysics).

Iron mineralization assays employed a higher iron to protein stoichiometry of 400 Fe^{2+} per *Syn*Ftn. Dependences of absorbance on time were recorded on a Hitachi U-2900 spectrometer following manual mixing of 6.4 μL of a 50 mM Fe^{2+} solution in 50 mM HCl to a 1.6-mL sample of 0.5 μM protein in 100 mM Mes, pH 6.5. Initial rates of iron mineralization were deduced from the gradient of the initial linear region and an extinction coefficient for the mineral core calculated from the net absorbance change upon complete oxidation of the 200 μM Fe^{2+} added (active proteins) or an assumed extinction coefficient for the core of 2,000 $M^{-1} \cdot cm^{-1}$ (E33A and E110A).

EPR Spectroscopy. EPR spectra were recorded at 10 K or at room temperature on a Bruker EMX (X-band) EPR spectrometer. Low-temperature measurements were performed with the use of an Oxford Instruments liquid-helium system and a spherical high-quality ER 4122 SP 9703 Bruker resonator. Protein samples in EPR tubes were mixed with the appropriate volume of a 25 mM stock Fe^{2+} solution and frozen at least 10 s thereafter by plunging the tubes into methanol cooled with solid CO_2. Samples frozen at times <10 s (the RFQ technique) were prepared by mixing equal volumes of an 8.33 μM protein solution (200 μM in subunit monomer) and a 0.6 mM Fe^{2+} solution in an Update Instrument 715 Syringe Ram Controller and ejecting the mixture onto the surface of a rapidly rotating aluminum disk maintained at liquid nitrogen temperature (54). Final protein concentration was 4.17 μM (100 μM in monomer) in all cases. Stopped-flow absorbance measurements performed at comparable protein concentration to RFQ EPR showed that at ambient temperature the rapid oxidation phase of wild-type *Syn*Ftn would be >50% complete in 50 ms, the shortest available freezing time, but that the rate of this phase could be slowed by lowering the reaction temperature (*SI Appendix*, Fig. S3*A*). Consequently, for RFQ measurements of wild-type *Syn*Ftn, the chamber housing the sample syringes was packed with a water/ice mixture. The equivalent measurements on variant Y40F were conducted at ambient temperature because it lacks a rapid oxidation phase, enabling a more reliable comparison with stopped-flow data.

Proteins were in 100 mM Mes, pH 6.5, and Fe^{2+} solutions in 50 mM HCl (slow freezing) or 1 mM HCl (RFQ). Instrument parameters for EPR measurements were as follows: microwave frequency ν_{MW} = 9.4657 GHz, modulation frequency ν_M = 100 kHz, time constant τ = 82 ms, microwave power = 3.19 or 0.05 mW (for 100-G-wide free-radical scans), modulation amplitude A_M = 5 or 3 G (for free-radical scans), and scan rate v = 22.6 or 0.6 $G \cdot s^{-1}$ (for free radicals). Quantification of paramagnetic species was achieved by comparison of integrated intensities to those of a 1 mM Cu[EDTA] solution (Tyr radical and MVFC) or a 35 μM solution of Fe^{3+} containing Ferric Binding Protein from *Neisseria gonorrhoeae* (high-spin mononuclear ferric iron with g = 4.3).

Room temperature EPR measurements were performed with the use of a Bruker AquaX system with a 4103TM Bruker resonator. A homemade mixing device was used to mix equal volumes of two liquid components and fill the AquaX capillary bundle. The dead volume of the mixing device was 130 μL and the minimal volume to be taken by each input syringe was 180 μL. The dead time of the mixing device was 2 s. DMPO (Sigma) was used to spin-trap short-lived radicals in the room temperature experiments. DMPO was dissolved in water at 228 mM concentration and filtered over activated charcoal. EPR spectra were recorded before and after this filtration step to measure the removal of paramagnetic impurities. In a typical experiment, a solution of protein with DMPO was mixed with equal volume of freshly prepared Fe^{2+} so that the final concentrations were as follows: 5.4 μM protein, 40 mM DMPO, 375 μM Fe^{2+}—in 100 mM Mes buffer, pH 6.5. The reference spectra of the superoxide radical DMPO adduct and hydroxyl radical DMPO adduct were obtained in a xanthine oxidase/xanthine system [0.16 units of xanthine oxidase (Sigma), 0.4 mM xanthine (Sigma), 100 mM DMPO—in 50 mM sodium phosphate buffer, pH 7.7] and in a Fenton reagent system (1 mM Fe^{2+}, 1 mM H_2O_2, 40 mM DMPO), respectively. Instrumental parameters were as follows: microwave frequency ν_{MW} = 9.799 GHz, microwave power = 12.57 mW, modulation frequency ν_M = 100 kHz, modulation amplitude A_M = 1 G, time constant μ = 40.96 ms, and scan rate v = 0.83 $G \cdot s^{-1}$.

Spectral simulations of MVFC EPR signals were performed using WinEPR SimFonia (Bruker Biospin) using the parameters reported in Table 1. The free-radical EPR spectra were simulated using SimPow6 (55), while the simulation parameters were found by using the TRSSA (29). Assignment of the radical in *Syn*Ftn to a specific tyrosine site was performed on the basis of correspondence drawn between the rotation angle in the phenoxyl ring in the radical, found from the simulation, and the angles of the ring in the tyrosine residues as seen in the crystal structure. The analysis of these angles is reported in *SI Appendix*, Table S5.

Oximetry Measurements. The stoichiometry of the *Syn*Ftn-catalyzed iron–O_2 reaction was deduced by monitoring the decrease in the dissolved O_2 concentration in a 1 μM solution of protein in 2 mL of 100 mM Mes, pH 6.5, following additions of 4-μL aliquots of 24 mM Fe^{2+} in 50 mM HCl (48 μM final concentration) using a Clark electrode (Hansatech Instruments Oxygraph$^+$). The iron:O_2 ratios reported are the mean of three independent measurements under each reaction condition together with the SEM. The ability of *Syn*Ftn to reduce O_2 at the surface of a growing mineral core was assessed by adding 33 μL of 24 mM Fe^{2+} to apo protein as above (400 Fe^{2+}/*Syn*Ftn). Reaction was judged complete once the O_2 concentration became invariant within error for 20 s and a further 4 μL of Fe^{2+} added.

Detection of Hydrogen Peroxide. Release of H_2O_2 was detected using the Amplex Red assay (Thermo Fisher Scientific). The 560-nm absorbance of samples containing 0.1 μM wild-type or Y40F *Syn*Ftn, incubated with varying ratios (24–72 equivalents) of Fe^{2+}, were compared with a standard plot ($y = 0.009x + 0.0379$, $R^2 = 0.997$) constructed using 0–5 μM H_2O_2 prepared from dilution of a 20 mM standard solution into identical buffer (sodium phosphate, pH 7.4).

***Syn*Ftn Interactions with Copper.** The possibility of copper binding to *Syn*Ftn was investigated under two conditions. Direct interaction with *Syn*Ftn was probed by incubating 0.5 μM protein with 200 μM copper either added aerobically as Cu^{2+} or anaerobically as Cu^+ for 60 min. Separate samples containing Cu^+ were either maintained in an anaerobic environment or exposed to O_2 during incubation. Weakly associated or unbound copper was then removed using a desalting column (Sephadex G-25M; GE Healthcare). The 0.5-mL aliquots of the eluted sample were then digested by mixing with an equal volume of 68% HNO_3 and heating to 80 °C for 16 h. Cooled samples were neutralized by adding 2.5 mL of saturated sodium acetate and incubated at 37 °C for 15 min following the addition of 0.5 mL each of NH_2OH (3.2 $mg \cdot mL^{-1}$) and bathocuproinedisulfonic acid (BCS) (5.0 mg mL^{-1}). Copper content was determined by comparison of the absorbance at 484 nm to a standard plot constructed using copper solutions (0–100 μM) treated identically to protein solutions eluted from the G-25 column ($y = 0.0014x - 0.0034$, $R^2 = 0.998$). The same assay was used to probe incorporation of copper into the mineral core during deposition but with 4.1 μM *Syn*Ftn incubated aerobically with 1.6 mM Fe^{2+} and 200 μM of either Cu^+ or Cu^{2+}.

Absorbance monitored mineralization assays conducted on 0.5 μM protein demonstrated that incorporation of iron into the protein core proceeds at 90% of the rate observed in the absence of copper. A standard plot constructed from solutions containing both Fe^{2+} and Cu^{2+} indicated that the presence of the former did not interfere with copper detection using BCS.

ACKNOWLEDGMENTS. We thank Dr. Nick Watmough (University of East Anglia) for access to the stopped-flow instrument, Prof. Dominic Campopiano (University of Edinburgh) for providing Ferric Binding Protein, and Prof. Michael Murphy (University of British Columbia) for providing *Pm*Ftn. This work was supported by the United Kingdom's Biotechnology and Biological Sciences Research Council through Grants BB/I021884/1 and BB/R002363/1, and National Science Foundation Grants MCB0744334 and DEB-1233085. A portion of this work was performed under the auspices of the US Department of Energy by Lawrence Livermore National Laboratory under Contract DE-AC52-07NA27344.

1. Le Brun NE, Crow A, Murphy MEP, Mauk AG, Moore GR (2010) Iron core mineralisation in prokaryotic ferritins. *Biochim Biophys Acta* 1800:732–744.
2. Theil EC, Behera RK, Tosha T (2013) Ferritins for chemistry and for life. *Coord Chem Rev* 257:579–586.
3. Briat JF, Duc C, Ravet K, Gaymard F (2010) Ferritins and iron storage in plants. *Biochim Biophys Acta* 1800:806–814.
4. Levi S, et al. (1992) Evidence of H- and L-chains have co-operative roles in the iron-uptake mechanism of human ferritin. *Biochem J* 288:591–596.
5. Bauminger ER, Harrison PM, Hechel D, Nowik I, Treffry A (1991) Mössbauer spectroscopic investigation of structure-function relations in ferritins. *Biochim Biophys Acta* 1118:48–58.
6. Bradley JM, Moore GR, Le Brun NE (2017) Diversity of Fe^{2+} entry and oxidation in ferritins. *Curr Opin Chem Biol* 37:122–128.
7. Pereira AS, et al. (1998) Direct spectroscopic and kinetic evidence for the involvement of a peroxodiferric intermediate during the ferroxidase reaction in fast ferritin mineralization. *Biochemistry* 37:9871–9876.
8. Li WKW (1994) Primary production of prochlorophytes, cyanobacteria and eukaryotic ultraphytoplankton—measurements from flow cytometric sorting. *Limnol Oceanogr* 39:169–175.
9. Stuart RK, Dupont CL, Johnson DA, Paulsen IT, Palenik B (2009) Coastal strains of marine *Synechococcus* species exhibit increased tolerance to copper shock and a distinctive transcriptional response relative to those of open-ocean strains. *Appl Environ Microbiol* 75:5047–5057.
10. Arosio P, Levi S (2002) Ferritin, iron homeostasis, and oxidative damage. *Free Radic Biol Med* 33:457–463.
11. Christie-Oleza JA, Armengaud J, Guerin P, Scanlan DJ (2015) Functional distinctness in the exoproteomes of marine *Synechococcus*. *Environ Microbiol* 17:3781–3794.
12. Bou-Abdallah F, et al. (2014) Functionality of the three-site ferroxidase center of *Escherichia coli* bacterial ferritin (EcFtnA). *Biochemistry* 53:483–495.
13. Tatur J, Hagedoorn PL, Overeijnder ML, Hagen WR (2006) A highly thermostable ferritin from the hyperthermophilic archaeal anaerobe *Pyrococcus furiosus*. *Extremophiles* 10:139–148.
14. Baaghil S, Thomson AJ, Moore GR, Le Brun NE (2002) Studies of copper(II)-binding to bacterioferritin and its effect on iron(II) oxidation. *J Chem Soc Dalton Trans* 2002:811–818.
15. Bertini I, et al. (2012) Structural insights into the ferroxidase site of ferritins from higher eukaryotes. *J Am Chem Soc* 134:6169–6176.
16. Bossek U, Hummel H, Weyhermuller T, Bill E, Wieghardt K (1995) The first μ(OH)-bridged model complex for the mixed-valent Fe(III)-Fe(II) form of hemerythrin. *Angew Chem Int Ed Engl* 34:2642–2645.
17. Pfaffen S, Abdulqadir R, Le Brun NE, Murphy MEP (2013) Mechanism of ferrous iron binding and oxidation by ferritin from a pennate diatom. *J Biol Chem* 288:14917–14925.
18. Lawson TL, et al. (2009) Monitoring the iron status of the ferroxidase center of *Escherichia coli* bacterioferritin using fluorescence spectroscopy. *Biochemistry* 48:9031–9039.
19. Pozzi C, et al. (2015) Iron binding to human heavy-chain ferritin. *Acta Crystallogr D Biol Crystallogr* 71:1909–1920.
20. Tatur J, Hagen WR (2005) The dinuclear iron-oxo ferroxidase center of *Pyrococcus furiosus* ferritin is a stable prosthetic group with unexpectedly high reduction potentials. *FEBS Lett* 579:4729–4732.
21. Honarmand Ebrahimi K, Bill E, Hagedoorn PL, Hagen WR (2012) The catalytic center of ferritin regulates iron storage via Fe(II)-Fe(III) displacement. *Nat Chem Biol* 8:941–948.
22. Li F, et al. (2012) Structural, EPR, and Mössbauer characterization of (μ-alkoxo)(μ-carboxylato)diiron(II,III) model complexes for the active sites of mixed-valent diiron enzymes. *Inorg Chem* 51:2917–2929.
23. Yang X, Chen-Barrett Y, Arosio P, Chasteen ND (1998) Reaction paths of iron oxidation and hydrolysis in horse spleen and recombinant human ferritins. *Biochemistry* 37:9743–9750.
24. Pozzi C, et al. (2015) Time-lapse anomalous X-ray diffraction shows how Fe^{2+} substrate ions move through ferritin protein nanocages to oxidoreductase sites. *Acta Crystallogr D Biol Crystallogr* 71:941–953.
25. Elgren TE, et al. (1991) Electron transfer associated with oxygen activation in the B2 protein of ribonucleotide reductase from *Escherichia coli*. *J Biol Chem* 266:19265–19268.
26. Giese B, Graber M, Cordes M (2008) Electron transfer in peptides and proteins. *Curr Opin Chem Biol* 12:755–759.
27. Bradley JM, et al. (2015) Three aromatic residues are required for electron transfer during iron mineralization in bacterioferritin. *Angew Chem Int Ed Engl* 54:14763–14767.
28. Ebrahimi KH, Hagedoorn PL, Hagen WR (2013) A conserved tyrosine in ferritin is a molecular capacitor. *Chembiochem* 14:1123–1133.
29. Svistunenko DA, Cooper CE (2004) A new method of identifying the site of tyrosyl radicals in proteins. *Biophys J* 87:582–595.
30. Hemmings AM, et al. (2017) Metal free structure of Y40F *Syn*Ftn. Protein Data Bank. Available at https://www.rcsb.org/structure/5OUZ. Deposited August 8, 2017.
31. Hemmings AM, et al. (2018) Iron soak structure of Y40F *Syn*Ftn. Protein Data Bank. Available at https://www.rcsb.org/structure/6GKB. Deposited May 17, 2018.
32. Pearce LL, Kurtz DM, Xia YM, Debrunner PG (1987) Reduction of the binuclear iron site in octameric methemerythrins—characterizations of intermediates and a unifying reaction scheme. *J Am Chem Soc* 109:7286–7293.
33. Lauffer RB, Antanaitis BC, Aisen P, Que L, Jr (1983) ^{1}H NMR studies of porcine uteroferrin. Magnetic interactions and active site structure. *J Biol Chem* 258:14212–14218.
34. Smoukov SK, et al. (2003) EPR and ENDOR evidence for a 1-His, hydroxo-bridged mixed-valent diiron site in *Desulfovibrio vulgaris* rubrerythrin. *Biochemistry* 42:6201–6208.
35. Davydov RM, et al. (1997) EPR study of the mixed-valent diiron sites in mouse and herpes simplex virus ribonucleotide reductases. Effect of the tyrosyl radical on structure and reactivity of the diferric center. *Biochemistry* 36:9093–9100.
36. Davydov R, Valentine AM, Komar-Panicucci S, Hoffman BM, Lippard SJ (1999) An EPR study of the dinuclear iron site in the soluble methane monooxygenase from *Methylococcus capsulatus* (Bath) reduced by one electron at 77 K: The effects of component interactions and the binding of small molecules to the diiron(III) center. *Biochemistry* 38:4188–4197.
37. Xing G, et al. (2006) Evidence for C–H cleavage by an iron-superoxide complex in the glycol cleavage reaction catalyzed by myo-inositol oxygenase. *Proc Natl Acad Sci USA* 103:6130–6135.
38. Wörsdörfer B, et al. (2013) Organophosphonate-degrading PhnZ reveals an emerging family of HD domain mixed-valent diiron oxygenases. *Proc Natl Acad Sci USA* 110:18874–18879.
39. Jasniewski AJ, Que L, Jr (2018) Dioxygen activation by nonheme diiron enzymes: Diverse dioxygen adducts, high-valent intermediates, and related model complexes. *Chem Rev* 118:2554–2592.
40. Sazinsky MH, Lippard SJ (2006) Correlating structure with function in bacterial multicomponent monooxygenases and related diiron proteins. *Acc Chem Res* 39:558–566.
41. Trehoux A, Mahy JP, Avenier F (2016) A growing family of O$_2$ activating dinuclear iron enzymes with key catalytic diiron(III)-peroxo intermediates: Biological systems and chemical models. *Coord Chem Rev* 322:142–158.
42. Xing G, et al. (2006) A coupled dinuclear iron cluster that is perturbed by substrate binding in myo-inositol oxygenase. *Biochemistry* 45:5393–5401.
43. Macomber L, Imlay JA (2009) The iron-sulfur clusters of dehydratases are primary intracellular targets of copper toxicity. *Proc Natl Acad Sci USA* 106:8344–8349.
44. Dufresne A, Garczarek L, Partensky F (2005) Accelerated evolution associated with genome reduction in a free-living prokaryote. *Genome Biol* 6:R14.
45. Honarmand Ebrahimi K, Hagedoorn PL, Hagen WR (2015) Unity in the biochemistry of the iron-storage proteins ferritin and bacterioferritin. *Chem Rev* 115:295–326.
46. Winter G (2010) XIA2: An expert system for macromolecular crystallography data reduction. *J Appl Cryst* 43:186–190.
47. Evans PR (2011) An introduction to data reduction: Space-group determination, scaling and intensity statistics. *Acta Crystallogr D Biol Crystallogr* 67:282–292.
48. Winn MD, et al. (2011) Overview of the CCP4 suite and current developments. *Acta Crystallogr D Biol Crystallogr* 67:235–242.
49. Afonine PV, et al. (2012) Towards automated crystallographic structure refinement with phenix.refine. *Acta Crystallogr D Biol Crystallogr* 68:352–367.
50. Stillman TJ, et al. (2001) The high-resolution X-ray crystallographic structure of the ferritin (EcFtnA) of *Escherichia coli*; comparison with human H ferritin (HuHF) and the structures of the Fe^{3+} and Zn^{2+} derivatives. *J Mol Biol* 307:587–603.
51. Emsley P, Lohkamp B, Scott WG, Cowtan K (2010) Features and development of Coot. *Acta Crystallogr D Biol Crystallogr* 66:486–501.
52. Handing KB, et al. (2018) Characterizing metal-binding sites in proteins with X-ray crystallography. *Nat Protoc* 13:1062–1090.
53. Zheng H, et al. (2014) Validation of metal-binding sites in macromolecular structures with the CheckMyMetal web server. *Nat Protoc* 9:156–170.
54. Thompson MK, Franzen S, Ghiladi RA, Reeder BJ, Svistunenko DA (2010) Compound ES of dehaloperoxidase decays via two alternative pathways depending on the conformation of the distal histidine. *J Am Chem Soc* 132:17501–17510.
55. Nilges MJ, Mattson K, Belford RL (2007) Simpow6: A software package for the simulation of ESR powder-type spectra. *ESR Spectrosc Membr Biophys* 27:261–281.
56. Hemmings AM, et al. (2017) Metal free structure of *Syn*Ftn. Protein Data Bank. Available at https://www.rcsb.org/structure/5OUW. Deposited August 4, 2017.
57. Hemmings AM, et al. (2018) 2 minute Fe^{2+} soak of *Syn*Ftn. Protein Data Bank. Available at https://www.rcsb.org/structure/6GKC. Deposited May 17, 2018.
58. Hemmings AM, et al. (2018) 20 minute Fe^{2+} soak of *Syn*Ftn. Protein Data Bank. Available at https://www.rcsb.org/structure/6GKA. Deposited May 18, 2018.